

Probabilistic assessment of potential fault slip related to injection-induced earthquakes: Application to north-central Oklahoma, USA

F. Rall Walsh, III, and Mark D. Zoback

Department of Geophysics, Stanford University, 397 Panama Mall, Stanford, California 94305, USA

ABSTRACT

We utilize quantitative risk assessment (QRA) to calculate the conditional probability of slip on mapped faults in response to injection-related increases in pore pressure in north-central Oklahoma (USA) where widespread injection of produced saltwater has triggered thousands of small to medium-sized earthquakes in the past 7 yr. The conditional probability incorporates the uncertainty in each Mohr-Coulomb parameter (stress tensor, pore pressure, coefficient of friction, and fault orientation) through QRA. The result is a cumulative distribution function of the pore pressure required to cause slip on each fault segment. The results can be used to assess the probability of induced slip on a known fault from a given injection-related pore pressure increase. After dividing north-central Oklahoma into six study areas, we invert earthquake focal plane mechanisms in each area to constrain the orientation and relative magnitude of the principal stresses. The QRA identifies the potential for slip on the fault that produced the M 5.6 Prague earthquake in 2011 and the northeastern extension of a mapped fault associated with the M 5.1 Fairview earthquake sequence that occurred in early 2016, and, had the 289° -striking fault of the September 2016 M 5.8 Pawnee event been mapped, it would have been identified as potentially active.

INTRODUCTION

One mechanism by which injection-related pore pressure increases can trigger seismic slip is well understood in the context of Mohr-Coulomb failure criteria (e.g., National Research Council, 2013). Wastewater disposal has been associated with induced earthquakes at a number of sites in the central and eastern United States (Horton, 2012; Keranen et al., 2013). In north-central Oklahoma, the increase in seismicity that began in 2009 (Fig. 1) is caused by large rates of produced-saltwater disposal in the area where the earthquakes are occurring (Walsh and Zoback, 2015). We present a methodology to quantify the conditional probability of inducing slip on known faults in response to injection-related pore pressure changes given reasonable assumptions using a Mohr-Coulomb slip criteria. While other physical processes can affect triggering, we identify the faults of most concern.

We first review existing information on faults in Oklahoma. We then discuss the available earthquake focal mechanisms within each of six study areas to constrain the stress field in each area. The study areas are defined to encompass most of the recent seismicity and the best seismic coverage (McNamara et al., 2015). The focal mechanism inversions yield information about both stress orientation and relative magnitudes. We next demonstrate how quantitative risk assessment (QRA) can be used to assess the conditional probability that a known fault might slip in response to injected-related pore pressure increases through a Mohr-Coulomb mechanism.

A key component of this analysis is constraining the uncertainties associated with each of the geomechanical parameters. It should be noted that within the seismic hazard community, the term “risk” has a specific definition that incorporates seismic hazard, exposure, and the vulnerability of the community and structures affected by shaking. In our use of the term “QRA”, we are actually assessing the conditional probability of fault slip, which is, strictly speaking, related only to seismic hazard.

FAULTS

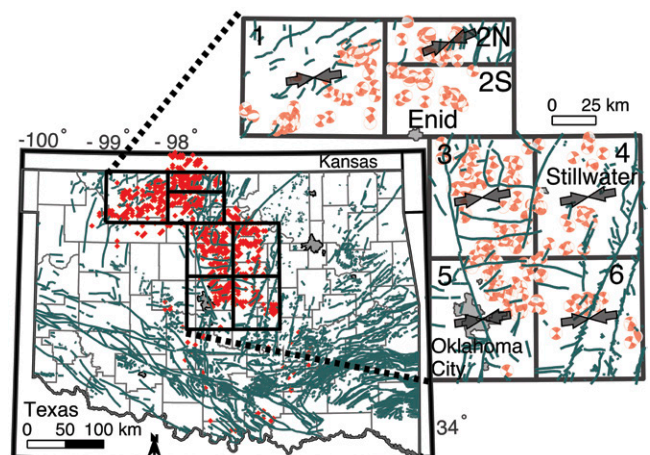
The map in Figure 1 shows fault segments compiled from published sources and information

donated by petroleum operators (Darold and Holland, 2015). The database contains 26,313 fault segments, each defined by two connected coordinate points. No information about fault dip or depth is included. The fault map is complete to varying degrees, as areas of tectonic uplift expose faults at the surface and sediments conceal them, unless known from wells or seismic data. This results in fewer mapped faults in the study areas considered here (as 2–3 km of sedimentary rock overlies crystalline basement), but the earthquakes in these areas are evidence that the lack of mapped faults is a reflection of undersampling, not the absence of faulting. The majority of earthquakes in north-central Oklahoma are at 5–6 km depth (McNamara et al., 2015), ~2–4 km into crystalline basement where faults are difficult to image. As can be inferred from the distribution of $M \geq 2.9$ focal plane mechanisms shown in the Figure 1 inset, the majority of the earthquakes are not associated with mapped faults. To calculate the probability of fault slip in a given stress field, we need information about both fault strike and dip, ideally its actual three-dimensional geometry. In the absence of dip information, we consider a probabilistic distribution of dips.

INVERTING MOMENT TENSORS FOR THE TECTONIC STRESS FIELD

We characterize the stress field in the study areas utilizing 335 focal plane mechanisms

Figure 1. Mapped Oklahoma (central USA) faults (gray lines; Darold and Holland, 2015) and M 3+ earthquakes that have occurred since 2009 (red dots; U.S. Geological Survey National Earthquake Information Center [NEIC] catalog [<http://earthquake.usgs.gov/earthquakes/>]). Six numbered study areas are discussed below. Area 2 was subdivided into northern (2N) and southern (2S) area. Inset shows moment tensors used in stress inversion in each study area. Gray arrows show azimuth of maximum horizontal compressive stress from moment tensor inversion within each study area.



from the St. Louis University Moment Tensor program (Herrmann, 2016), determined by waveform modeling, and from the U.S. Geological Survey National Earthquake Information Center (NEIC) catalog (<http://earthquake.usgs.gov/earthquakes/>). Each focal mechanism provides the strike, dip, and rake of two nodal planes, one of which represents the slip plane and the other an auxiliary nodal plane. We constrain the tectonic stress orientations and relative magnitudes using a linearized inversion of focal plane mechanisms (after Michael, 1984). Ideally, one would invert at least 25–30 well-constrained focal mechanisms per area (Townend and Zoback, 2001). Thus, there is a trade-off between the size of the area selected and the number of focal mechanisms in each area that are available to constrain inversions.

Following Angelier (1990), we represent the relative magnitudes of the principal stresses with the parameter ϕ which is defined by the magnitude of the intermediate principal stress (S_2) with respect to the maximum (S_1) and minimum (S_3) principal stresses:

$$\phi = (S_2 - S_3) / (S_1 - S_3). \quad (1)$$

When combined with the orientation of the principal stresses, the ϕ value describes the style of faulting in a given area. Table DR1 in the GSA Data Repository¹ presents a summary of the stress inversion results. We also show in the Data Repository the convergence and decrease of uncertainty of the stress orientation and ϕ values for each of the six study areas as focal mechanisms are added to the inversion. Consistent values of stress orientation and relative magnitude are obtained in each area, and there is typically $<5^\circ$ between the stress orientation obtained by the inversion of the earthquake moment tensors and independent wellbore stress information in each study area (Alt and Zoback, 2014; Heibach et al., 2010). The stress field in area 2 appears to be more complex than those of the other areas, and therefore area 2 was split into a northern (area 2N) and southern area (area 2S), each with a comparable number of moment tensors. In area 2S, the focal mechanism inversions do not match the orientation of maximum horizontal stress from wellbores (Fig. DR4 in the Data Repository) nor the focal mechanism inversions in the surrounding areas. This discrepancy may reflect that there are not a sufficient number of focal mechanisms to satisfactorily constrain the stress in area 2S or that there are localized variations of the stress field. Whatever the reason, we do not have confidence

that the stress field is sufficiently constrained in area 2S to analyze it.

While the orientation of maximum horizontal stress, S_{Hmax} , throughout central Oklahoma is fairly uniform (Fig. 1), relative stress magnitudes vary. Study areas 3, 4, 5, and 6 are characterized by strike-slip faulting ($S_{Hmax} > S_{Vertical} > S_{Hmin}$; $Hmin$ is minimum horizontal), areas 1 and 2S are characterized by both strike-slip and normal faulting ($S_{Hmax} \approx S_{Vertical} > S_{Hmin}$), and area 2N, much like southern Kansas (Rubinstein et al., 2015), is characterized predominantly by normal faulting ($S_{Vertical} > S_{Hmax} > S_{Hmin}$). We bootstrap the moment tensor inversion to constrain the uncertainty in stress orientation and ϕ value that we input into the QRA.

THE PROBABILITY OF TRIGGERED FAULT SLIP

In the context of Coulomb faulting theory, determining whether a fault will slip in response to fluid injection depends on the magnitude and orientation of the stress field, the orientation of the fault, pore pressure, and material parameters such as the coefficient of friction. Because there is uncertainty in each of these parameters, we evaluate the possibility that the mapped faults might slip in response to pore pressure increases using QRA, a Monte Carlo method used to evaluate the probability of an uncertain outcome incorporating uncertainty in the input parameters. In applied rock mechanics, QRA has been used to evaluate wellbore stability (Moos et al., 2003) and fault seal (Jones and Hillis, 2003). Leakage

of CO_2 from carbon sequestration reservoirs through wells, faults, and fractured caprock was investigated using QRA by Chae and Lee (2015). Chiaramonte et al. (2007) used QRA to evaluate if increases in pore pressure from a CO_2 injection pilot project might induce fault slip. The Chiaramonte et al. (2007) analysis assumed either purely strike-slip or normal faulting and only considered uncertainty in fault orientation. In this study, we generalize the QRA to include potential slip in any direction on mapped faults from uncertain stresses. Use of QRA is essential as there is uncertainty in all of the model parameters and no information available on mapped fault dip.

Figure 2 shows the distributions of ϕ , friction, pore pressure, and stress used in the QRA of study area 6. Similar figures for the other study areas are included in the Data Repository, as well as how the uncertainty in each parameter is established and a table of values. Figures 2C and 2D also show response surfaces in red, which use the most likely value in each distribution in Figure 2 (indicated by the vertical dotted black lines in the other distributions) to show the required pore pressure to induce fault slip based on a fault's dip (Fig. 2C) or strike (Fig. 2D). The black horizontal line in Figures 2C and 2D shows the 2 MPa expected pore pressure perturbation. This magnitude is based on Nelson et al. (2015) and the fact that wellhead pressures remain subhydrostatic after injection stops. Note that few fault strikes are present in study area 6 that would be expected to slip in response to a 2 MPa pore pressure change.

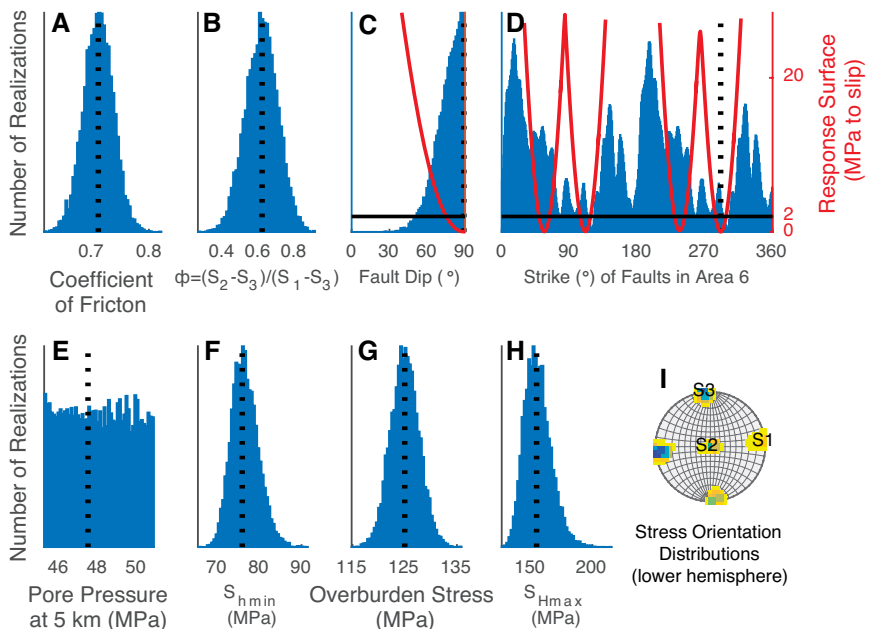


Figure 2. Distributions of parameters used in 10,000 calculations of pore pressure required to cause slip on each fault segment in study area 6 (Oklahoma, central USA; see Fig. 1 for location). Distributions of results from the bootstrapped moment tensor inversion are shown in B and I. Red (in C and D) show response surfaces of pore pressure to slip in the preferred geomechanical model described by vertical dotted black line in each parameter distribution. S_{Hmin} and S_{Hmax} —minimum and maximum horizontal stress.

¹GSA Data Repository item 2016334, uncertainty distributions (as in Figure 2) and probabilistic results (as in Figure 3), as well as focal mechanism inversions through time for each study area, is available online at www.geosociety.org/pubs/ft2016.htm or on request from editing@geosociety.org.

RESULTS OF THE QRA

In Figure 3, we apply QRA to the mapped faults in study area 6 utilizing the uncertainty distributions shown in Figure 2. As with the bootstrap of the moment tensor inversions, we evaluate 10,000 random combinations of parameters for each mapped fault segment to evaluate the conditional probability of slip as a function of pore pressure perturbation given the model assumptions described above in the context of Mohr-Coulomb faulting theory. We present the result as an empirical cumulative distribution function (CDF) showing the probability of slip on a known fault as a function of pore pressure increase. In Figure 3A, we map 484 fault segments in area 6 colored by their corresponding curves in Figure 3B. Figure 3B shows the probability of fault slip as a function of pore pressure change. We use a traffic-light color scale where fault segments with <1% conditional probability of slip in response to a 2 MPa pressure perturbation are colored green. Those with a >33% conditional probability are colored red. The large north-northeast–striking Wilzetta fault is colored green in Figure 3 as it strikes at too high an angle to the direction of maximum horizontal compression to be activated by a relatively small pore pressure perturbation. The Wilzetta splay fault just west of Prague (source of the 2011 M 5.6 earthquake) is colored red and would have had nearly a 50% probability of slip in response to a 2 MPa pressure perturbation. Note that there are other mapped potentially active faults. Maps and CDF curves similar to those in Figure 3 for each of the other study areas are presented in the Data Repository.

Figure 4 maps the probability of fault slip in response to a 2 MPa pore pressure change in all six study areas and an indication of the style of faulting (strike-slip, strike-slip–normal, or normal faulting) based on the focal mechanism inversions as summarized in Table DR1. We observe that the majority of mapped faults are not likely to be activated by modest pore pressure changes. Figure 4 also maps *M* 3+ earthquakes and saltwater disposal wells that injected more than 300,000 barrels in any month from 2009 through 2014. The 13 February 2016 *M* 5.1 earthquake near Fairview, Oklahoma, is circled in the southwestern part of area 1. The focal mechanism of the earthquake indicates a steeply dipping, northeast-striking fault plane that aligns with similarly striking faults mapped to both the southwest and northeast of the epicenter, colored varying shades of yellow.

DISCUSSION

The results presented in Figures 3 and 4 show the conditional probability of fault slip, given the uncertainties in the model parameters. The conditional probability of fault slip differs from the probability of an earthquake on a given fault because we don't know where the fault is in the

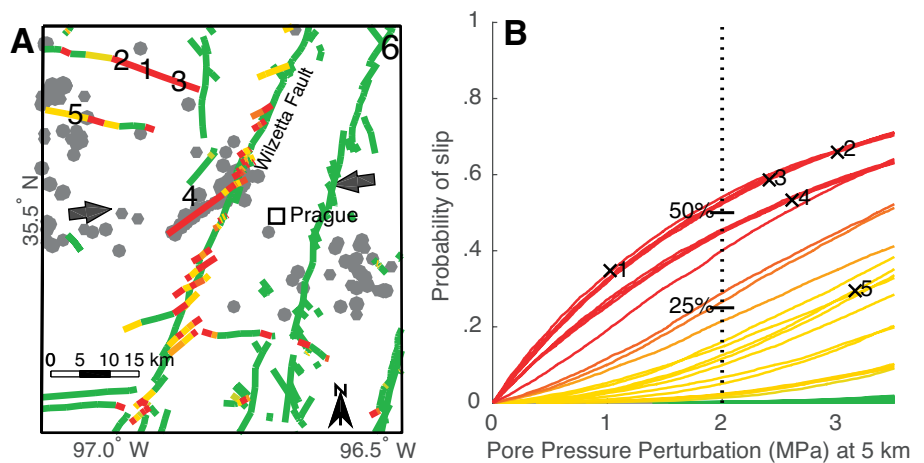


Figure 3. A: Study area 6 (Oklahoma, central USA; see Fig. 1 for location) showing mapped faults and U.S. Geological Survey National Earthquake Information Center (NEIC) catalog (<http://earthquake.usgs.gov/earthquakes/>) *M* 3+ earthquakes (gray dots). Selected faults are colored and numbered to correspond to their respective cumulative distribution function (CDF) shown in B. Colors of fault segments shown in A are based on corresponding CDF curves in B. **B:** CDF curves that are related to pore pressure changes similar to those expected during saltwater disposal.

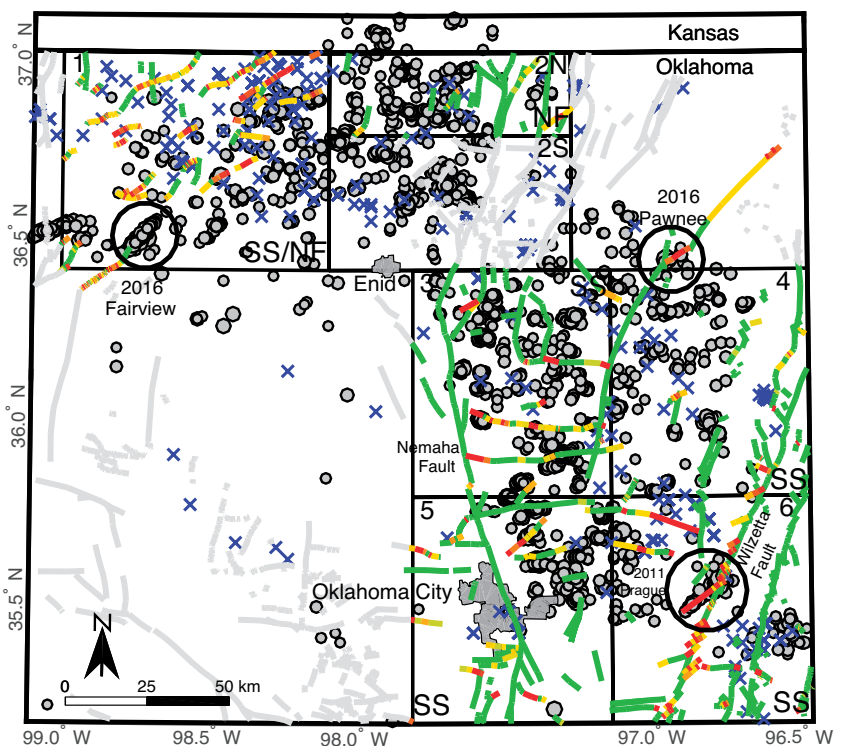


Figure 4. Fault map, with fault traces traffic-light colored by conditional probability of fault slip in response to pore pressure perturbations triggered by injection. Fault segments colored red represent >33% probability of slip in response to 2 MPa pore pressure perturbation; those in green represent <1% probability of slip in response to the same pressure. Gray dots show *M* 3+ earthquakes; gray lines show mapped faults that were not assessed. Disposal wells that injected >300,000 barrels in any month before 2015 are shown as blue x. SS—strike-slip faulting observed; NF—normal faulting observed. Large black circles show events >*M*5.

earthquake cycle. That is, we assume that if a fault is optimally oriented to slip in response to a 2 MPa pore pressure perturbation, it is likely to. However, had there been an earthquake on the fault in the past few thousand years, the stress drop in that earthquake might not have

recovered, reducing the probability of fault slip. Furthermore, our methodology considers the probability of fault slip, not the size of any possible earthquake. In other words, while large faults can produce larger earthquakes, the potential for slip over part (or all) of a fault is unknowable.

The San Andreas fault in California (USA) produces approximately one million $M \sim 2$ events for every $M \sim 8$ event. The fact that the majority of earthquakes are occurring on unmapped faults limits the applicability of our analysis to known faults and requires constraining other parameters such as the stress and pore pressure. We ignore poroelastic effects as these are likely to be minor in response to such small pore pressure changes. Similarly, while the Prague main shock may have been caused by a combination of static stress transfer from the $M 5$ foreshock and hydraulic triggering (Keranen et al., 2013), our analysis identifies that this fault could be triggered by a small perturbation.

We have taken a conservative approach to evaluating the potential for mapped fault slip in a Mohr-Coulomb framework. We also approach the magnitude of pore pressure changes in a conservative manner. In other words, assuming that an ~ 2 MPa pore pressure change is being transmitted throughout the region of seismicity and to the ~ 5 – 6 km depth of the earthquakes, we are considering a worst-case hydrologic scenario. It would be preferable to use constrained hydrologic modeling to assess the pore pressure change resulting from injection at the fault. As discussed by Keranen et al. (2014), this is difficult because many of the key hydrologic parameters are unknown. For example, if one were to assume injection is into a relatively isotropic, permeable medium, pore pressure would spread out uniformly from an injection well, and the pressure change at some distance could be estimated in a straightforward manner. However, permeability of faulted basement is likely to be complex. For example, some faults could be barriers to cross-fault flow but could have highly permeable damage zones that allow for rapid fluid pressure propagation parallel to the fault plane (e.g., Hennings et al., 2012). This complexity could result in relatively large pressure changes in some places at significant distance from injection wells (compared to what would be predicted from an isotropic permeability model) but smaller pressure changes in others.

CONCLUSIONS

We present a framework for calculating conditional probability of fault slip from a pore pressure perturbation by modeling Mohr-Coulomb slip, incorporating the uncertainties in relevant parameters. The application to induced seismicity in north-central Oklahoma confirms the potential for slip on the northeast-striking splay fault that produced the 2011 Prague earthquake but calculates a low probability of induced slip on several other large faults in the region (such as the Nemaha fault) in response to the relatively small pore pressure changes. The 2016 Fairview earthquake occurred on the previously

unmapped extension of a fault mapped as having moderate but varying probability of slip. Had the 289° -striking nodal plane of the focal mechanism of the $M 5.8$ Pawnee event been mapped, it would have been identified as a potentially active (red) fault.

The stress orientations obtained by inverting the focal mechanisms generally compare well with stress determinations made in wells in the same areas, building confidence in the inversions. The variation in stress has a significant effect on the orientation of potentially active faults within each area. This approach requires mapped faults, but the majority of the earthquakes in Oklahoma are on unmapped faults. It is also necessary to constrain the geomechanical parameters to assess the probability of injection-induced fault slip, and additional mechanisms could be considered. Despite these obstacles, this approach provides a rigorous quantification of mapped fault slip potential incorporating uncertainties in relevant parameters.

ACKNOWLEDGMENTS

The Stanford Center for Induced and Triggered Seismicity funded this work. We thank Stanford Professors Greg Beroza, Bill Ellsworth, and Jack Baker for helpful conversations, and Hiroki Sone for coding the Michael (1984) inversion and the resolving stress on fault codes. We also thank Peter Hennings, Cliff Frohlich, and one anonymous reviewer.

REFERENCES CITED

- Alt, R., and Zoback, M.D., 2014, Development of a detailed stress map of Oklahoma for avoidance of potentially active faults when siting wastewater injection wells: Abstract S51A-4434 presented at the 2014 Fall Meeting, American Geophysical Union, San Francisco, California, 15–19 December.
- Angelier, J., 1990, Inversion of field data in fault tectonics to obtain the regional stress—III. A new rapid direct inversion method by analytical means: *Geophysical Journal International*, v. 103, p. 363–376, doi:10.1111/j.1365-246X.1990.tb01777.x.
- Chae, K.S., and Lee, J.W., 2015, Risk analysis and simulation for geologic storage of CO_2 , in *Proceedings of the World Congress on Advances in Civil, Environmental, and Materials Research, Incheon, Korea, 25–29 August 2015*, 20 p.
- Chiaromonte, L., Zoback, M.D., Freidman, J., and Stamp, V., 2007, Seal integrity and feasibility of CO_2 sequestration in the Teapot Dome EOR pilot: *Geomechanical site characterization: Environmental Geology*, v. 54, p. 1667–1675, doi:10.1007/s00254-007-0948-7.
- Darold, A. P., and Holland, A. A., 2015, Preliminary Oklahoma optimal fault orientations: Oklahoma Geological Survey Open-File Report OF4-2015, scale 1:750,000.
- Hennings, P., et al., 2012, Relationship between fractures, fault zones, stress, and reservoir productivity in the Suban gas field, Sumatra, Indonesia: *American Association of Petroleum Geologists Bulletin*, v. 96, p. 753–772.
- Heidbach, O., Tingay, M., Barth, A., Reinecker, J., Kurfeß, D., and Müller, B., 2010, Global crustal stress pattern based on the World Stress Map database release 2008: *Tectonophysics*, v. 482, p. 3–15, doi:10.1016/j.tecto.2009.07.023.

- Herrmann, R., 2016, SLU North America Moment Tensor catalog in CSV format with TABS separating columns: http://www.eas.slu.edu/eqc/eqc_mt/MECH.NA/MECHFIG/mech.html (July 2016).
- Horton, S., 2012, Disposal of hydrofracking waste fluid by injection into subsurface aquifers triggers earthquake swarm in central Arkansas with potential for damaging earthquake: *Seismological Research Letters*, v. 83, p. 250–260, doi:10.1785/gssrl.83.2.250.
- Jones, R.M., and Hillis, R.R., 2003, An integrated, quantitative approach to assessing fault-seal risk: *American Association of Petroleum Geologists Bulletin*, v. 87, p. 507–524.
- Keranen, K.M., Savage, H.M., Abers, G.A., and Cochran, E.S., 2013, Potentially induced earthquakes in Oklahoma, USA: Links between wastewater injection and the 2011 $M_w 5.7$ earthquake sequence: *Geology*, v. 41, p. 699–702, doi:10.1130/G34045.1.
- Keranen, K.M., Weingarten, M., Abers, G.A., Bekins, B.A., and Ge, S., 2014, Sharp increase in central Oklahoma seismicity since 2008 induced by massive wastewater injection: *Science*, v. 345, p. 448–451, doi:10.1126/science.1255802.
- McNamara, D.E., Benz, H.M., Herrmann, R.B., Bergman, E.A., Earle, P., Holland, A.A., Baldwin, R., and Gassner, A., 2015, Earthquake hypocenters and focal mechanisms in central Oklahoma reveal a complex system of reactivated subsurface strike-slip faulting: *Geophysical Research Letters*, v. 42, p. 2742–2749, doi:10.1002/2014GL062730.
- Michael, A.J., 1984, Determination of stress from slip data: Faults and folds: *Journal of Geophysical Research*, v. 89, p. 11,517–11,526, doi:10.1029/JB089iB13p11517.
- Moos, D., Peska, P., Finkbeiner, T., and Zoback, M.D., 2003, Comprehensive wellbore stability analysis utilizing quantitative risk assessment: *Journal of Petroleum Science Engineering*, v. 38, p. 97–109, doi:10.1016/S0920-4105(03)00024-X.
- National Research Council, 2013, *Induced Seismicity Potential in Energy Technologies*: Washington, D.C., The National Academies Press, 262 p., doi:10.17226/13355.
- Nelson, P.H., Gianoutsos, N.J., and Drake, R.M., II, 2015, Underpressure in Mesozoic and Paleozoic rock units in the Midcontinent of the United States: *AAPG Bulletin*, v. 99, p. 1861–1892, doi:10.1306/04171514169.
- Rubinstein, J.L., Terra, F.M., and Ellsworth, W., 2015, Wastewater disposal, hydraulic fracturing, and seismicity in Southern Kansas: Abstract S22A-01 presented at the 2015 Fall Meeting, American Geophysical Union, San Francisco, California, 14–18 December.
- Townend, J., and Zoback, M.D., 2001, Implications of earthquake focal mechanisms for the frictional strength of the San Andreas fault system, in Holdsworth, R.E., et al., eds., *The Nature and Tectonic Significance of Fault Zone Weakening*: Geological Society of London Special Publication 186, p. 13–21, doi:10.1144/GSL.SP.2001.186.01.02.
- Walsh, F.R., and Zoback, M.D., 2015, Oklahoma's recent earthquakes and saltwater disposal: *Science Advances*, v. 1, e1500195, doi:10.1126/sciadv.1500195.

Manuscript received 21 June 2016

Revised manuscript received 14 September 2016

Manuscript accepted 16 September 2016

Printed in USA

SUPPLEMENTARY MATERIAL**Mohr-Coulomb Slip Calculation**

A recent summary of Mohr-Coulomb slip Criteria as it applies to injection induced seismicity, is available in (NRC 2012). For a given fault in a given stress field, we resolve the stress tensor on the fault, to calculate shear stress and normal stress. The Mohr-Coulomb slip failure criteria is our limit state function, which states that slip occurs if:

$$\tau \geq \mu (S_n - P_p)$$

where τ is the resolved shear stress on the fault, μ is the coefficient of friction, S_n is the normal (compressive) stress on the fault, and P_p is the pore pressure (Twiss and Moores, 1992). Thus in a deterministic way, we can straightforwardly calculate the pore pressure calculation that would be required to make an otherwise stable fault slip. In the QRA, we iterate the Mohr-Coulomb calculation with random samples from a distribution of each relevant parameter, reflecting its uncertainty. The distribution of outputs allows us to calculate the probability that a specific increase in pore pressure would cause fault slip. It should be noted that mechanisms of injection induced seismicity remain a field of ongoing research, and while we believe that this calculation is the simplest and most applicable, there are also other physical processes that could be relevant to triggering that we do not assess. These include poroelastic and thermoelastic stressing, rate and state-dependent frictional thresholds and stress-driven creep. It is also possible that faults have some cohesion, however it is unclear if it is significant when compared to uncertainty in friction coefficient and don't model it in this study, but it could be explicitly modeled in future work.

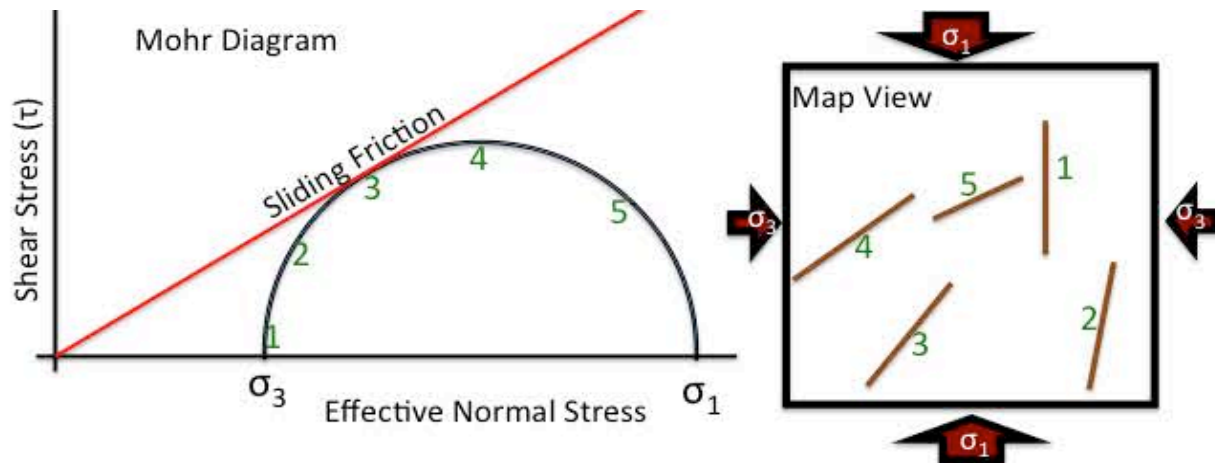


Figure DR1: 2D Mohr diagram showing 5 hypothetical faults in a 2D Mohr circle numbered to correspond to their orientations on the map. Fault number 3 is closest to slip in this stress field because the ratio of shear to effective normal stress is highest. Faults 2 and 4 could be triggered by modest changes in pore pressure, and faults 1 and 5 would require the most pore pressure to slip.

Application to Hydraulic Fracturing Seismicity

Although earthquakes of magnitude 2 and larger rarely occur during hydraulic fracturing, the methodology discussed here could also be used to assess the potential for fault slip during hydraulic fracturing (e.g. Friberg et al. 2015; Holland, 2013). Larger pore pressure perturbations would be expected during hydraulic fracturing operations than the < 2 MPa pore pressure change considered here for water disposal. To consider the probability that hydraulic fracturing might trigger slip, Fig. 3C considers the potential for slip on faults that might experience pressure changes as high as the magnitude of the least principal stress (sometimes referred to as the fracture gradient). Unlike saltwater disposal, hydraulic fracturing operations affect a small volume of rock for a short period of time. For example, during multi-stage hydraulic fracturing

in a horizontal well, it is typical to pressurize a ~100m long section of a well for about two hours.

Inversion of Moment Tensors for Stress

Study Area	S_{Hmax} Azimuth and Standard Deviation	ϕ	Number of Focal Mechanisms	Stress State
1	$83 \pm 2^\circ$	0.93 ± 0.04	65	Strike Slip and Normal Faulting
2N	$73 \pm 6^\circ$	0.65 ± 0.1	33	Normal Faulting
2S	NA	NA	33	Strike Slip and Normal Faulting
3	$82 \pm 1^\circ$	0.82 ± 0.04	132	Strike Slip Faulting
4	$82 \pm 4^\circ$	0.74 ± 0.12	28	Strike Slip Faulting
5	$83 \pm 2^\circ$	0.72 ± 0.06	51	Strike Slip Faulting
6	$84 \pm 2^\circ$	0.62 ± 0.09	26	Strike Slip Faulting

Table DR1: Moment Tensor inversion Results for each area.

Figures DR2-DR8 below show the evolution of S_{Hmax} azimuth (A) and ϕ (B) through time in each study area as more earthquakes occur. For a group of earthquake focal plane mechanisms, the inversion finds the best-fitting uniform stress orientation and relative magnitude by minimizing the misfit between the predicted and observed slip vectors on each of the nodal planes of the focal mechanism. The black line shows the deterministic result of 1 inversion of all moment tensors in the area up to that point in time, and the yellow to blue shows the density distribution of 1000 bootstrapped inversions of moment tensors up to that time. As more earthquakes occur with time, the inversion stabilizes (generally by 25-30 events), and the distribution and range of bootstrapped uncertainties tightens around the deterministic result. Also shown as magenta dashed lines (panel A) are the azimuths of S_{Hmax} from independent wellbore measurements (Alt and Zoback 2014, Heidbach et al. 2010) and the count of moment tensors through time in orange (right axis).

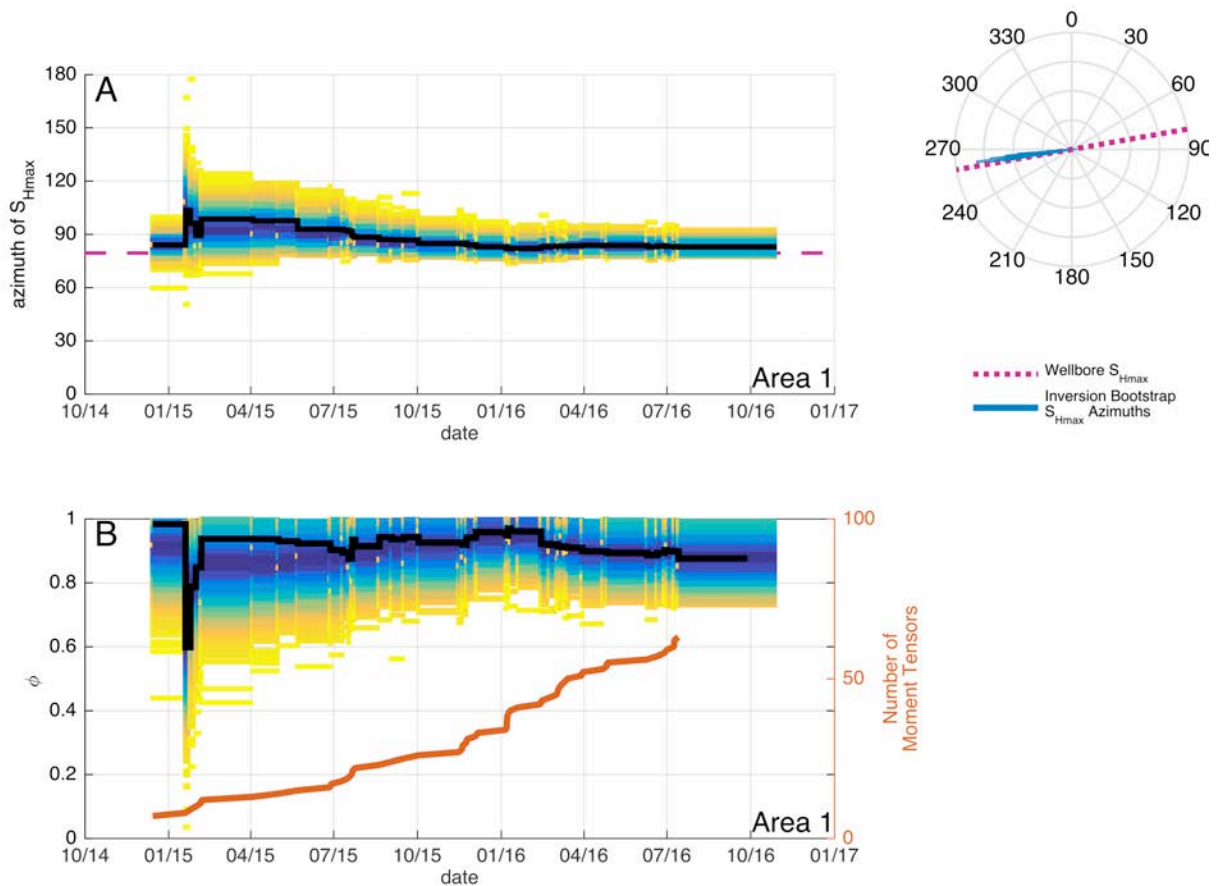


Figure DR2. Bootstrapped Inversion results through time as more earthquakes occur in area 1. Black is the deterministic inversion result, and blue-yellow shows the density of bootstrapped results through time. The magenta dashed line shows the S_{Hmax} azimuth from a wellbore measurement in area 1. The inversion converges to match the wellbore measurement. In DR2B, the orange line indicates the number of earthquakes with moment tensors used in the inversion as a function of time. A rose diagram is also shown with the final S_{Hmax} azimuths from the final bootstrapped results in blue, and the wellbore measurement as a magenta dashed line.

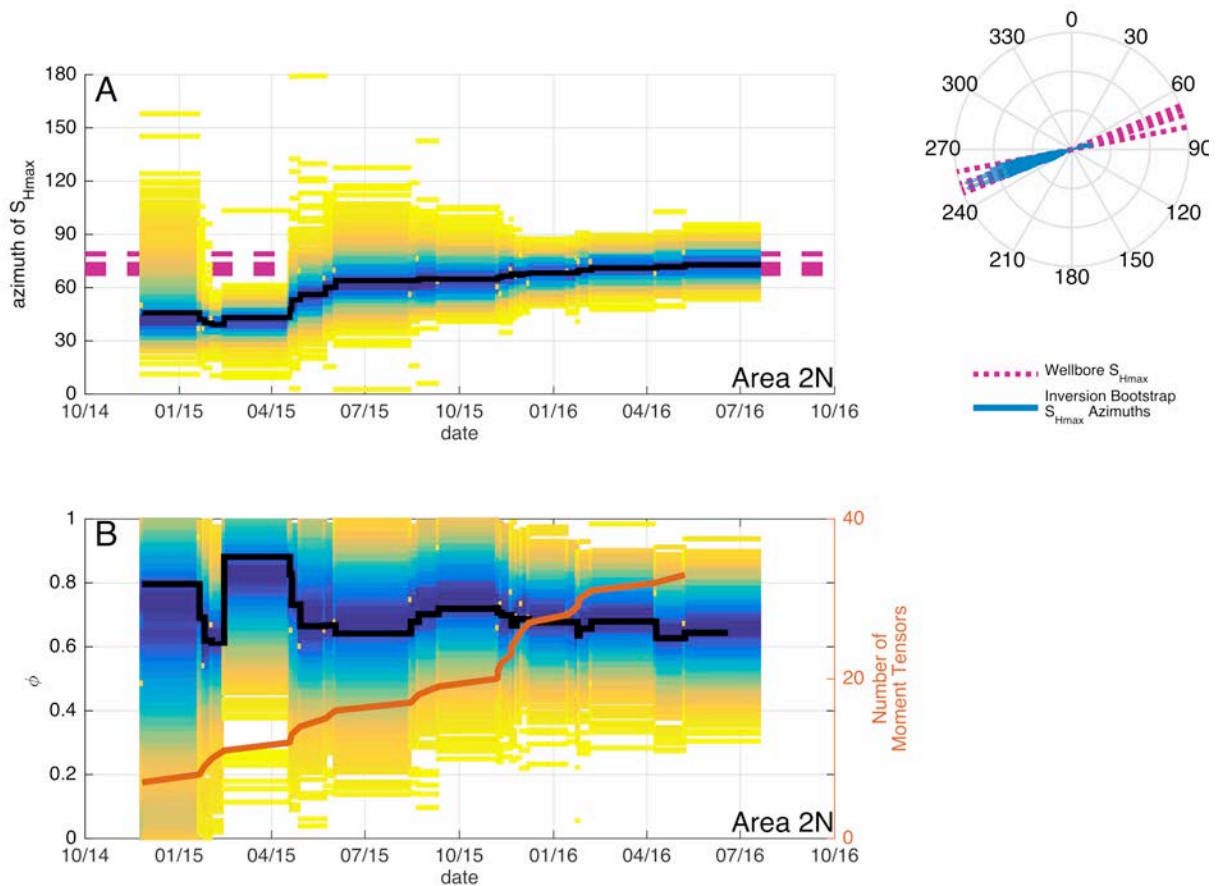


Figure DR3. Bootstrapped Inversion results through time as more earthquakes occur in area 2N. Black is the deterministic inversion result, and blue-yellow shows the distribution of bootstrapped results through time. The orange line indicates the number of earthquakes with moment tensors used in the inversion as a function of time. The horizontal magenta dashed lines show the S_{Hmax} azimuths from wellbore measurements. The inversion converges to match the wellbore measurements. A rose diagram is shown with the final S_{Hmax} azimuths from the final bootstrapped results in blue, and the wellbore measurements as magenta dashed lines.

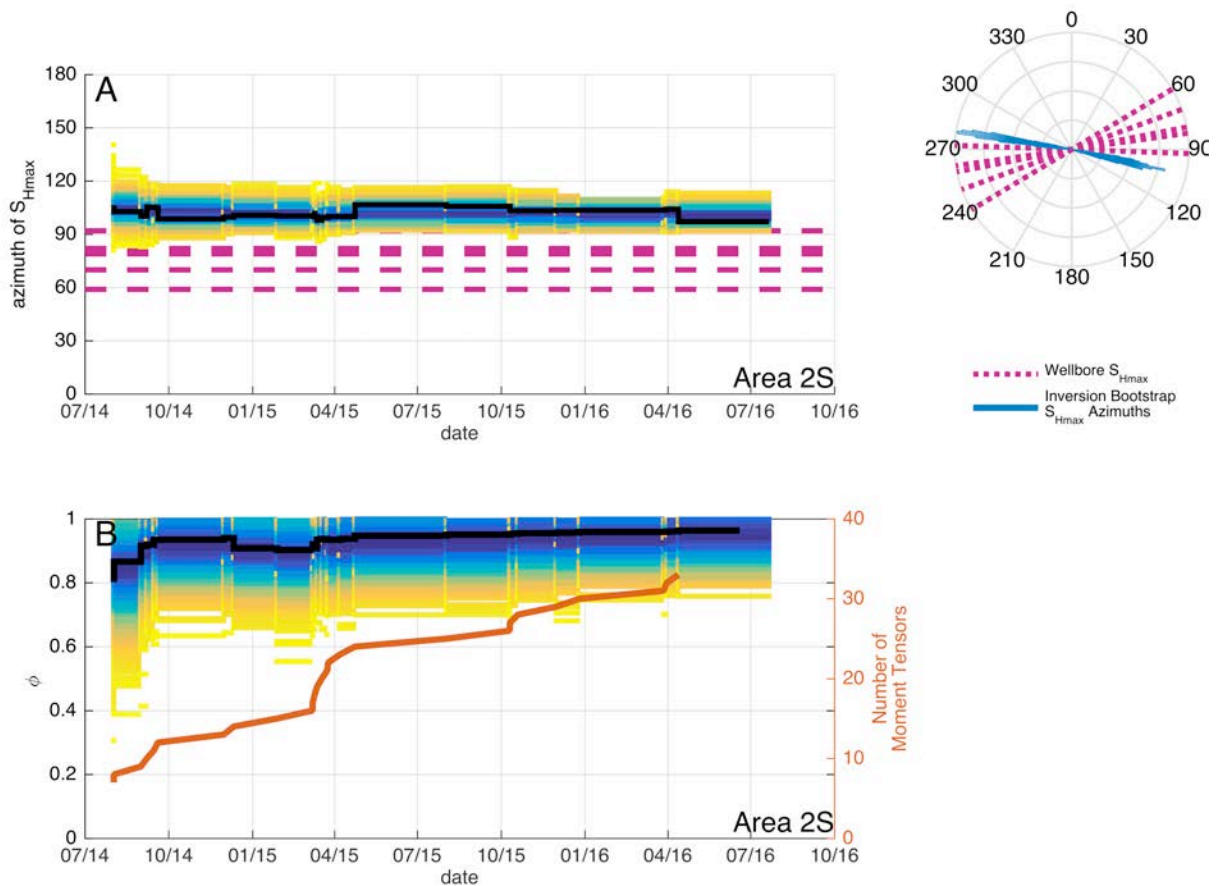


Figure DR4. Bootstrapped Inversion results through time as more earthquakes occur in area 2S. Black is the deterministic inversion result, and blue-yellow shows the distribution of bootstrapped results through time. The orange line indicates the number of earthquakes with moment tensors used in the inversion as a function of time. The horizontal magenta dashed lines show the S_{Hmax} azimuths from wellbore measurements (Alt and Zoback 2014, Heidbach et al. 2010). Here, the earthquake inversion does not converge to the wellbore measurements. A rose diagram is shown with the final S_{Hmax} azimuths from the final bootstrapped results in blue, and the wellbore measurements as magenta dashed lines, which clearly don't agree. This may be because the stress orientation changes with depth, as the earthquakes are considerably deeper than the wells, or because there are insufficient earthquakes in the inversion. Whatever the

reason, because the geomechanical uncertainties are large and the inversion can't be verified, we do not present fault results for this area in figure 4.

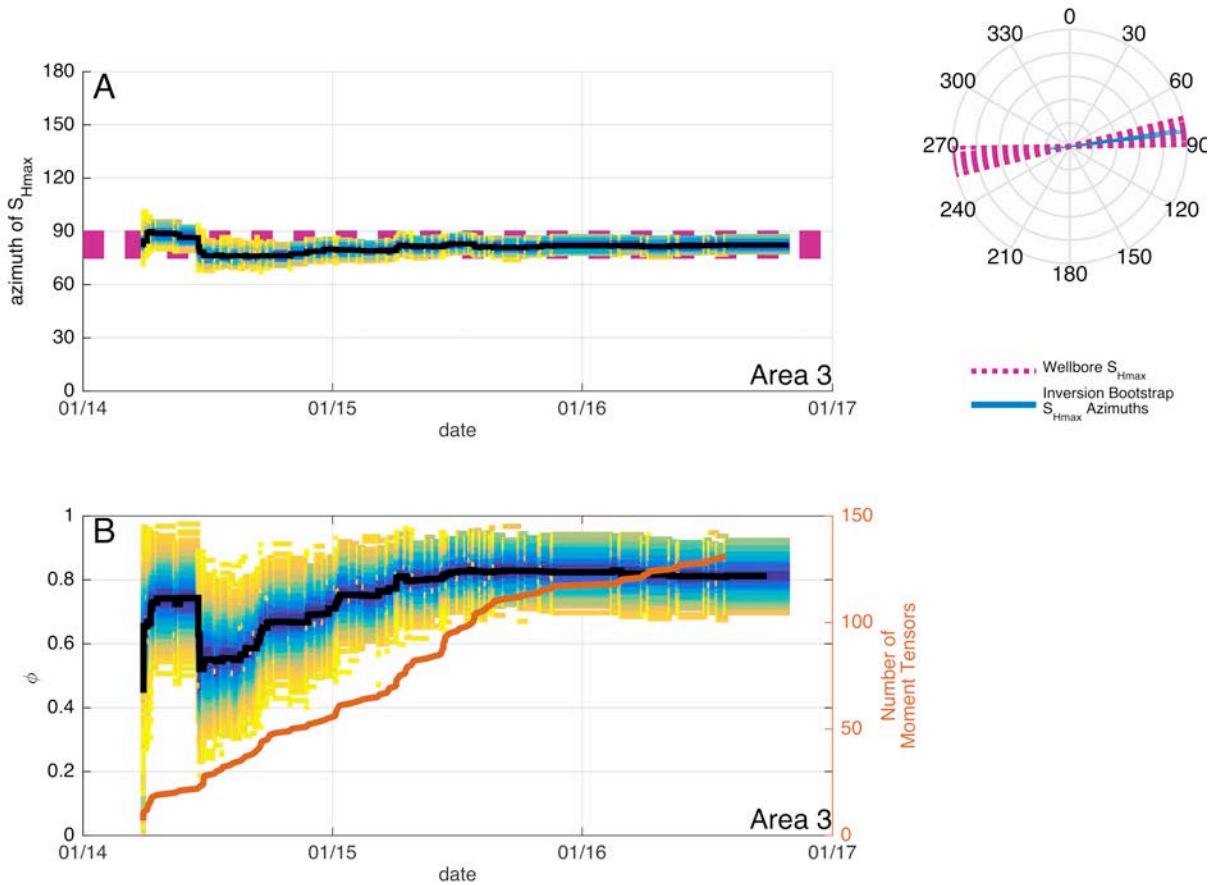


Figure DR5. Bootstrapped inversion results through time as more earthquakes occur in area 3. Black is the deterministic inversion result, and blue-yellow shows the distribution of bootstrapped results through time. The orange line indicates the number of earthquakes with moment tensors used in the inversion as a function of time. The horizontal magenta dashed line shows the S_{Hmax} azimuths from wellbore measurements. The inversion converges to match the wellbore measurements, and here the wellbore measurements have a greater variation than the inversions.

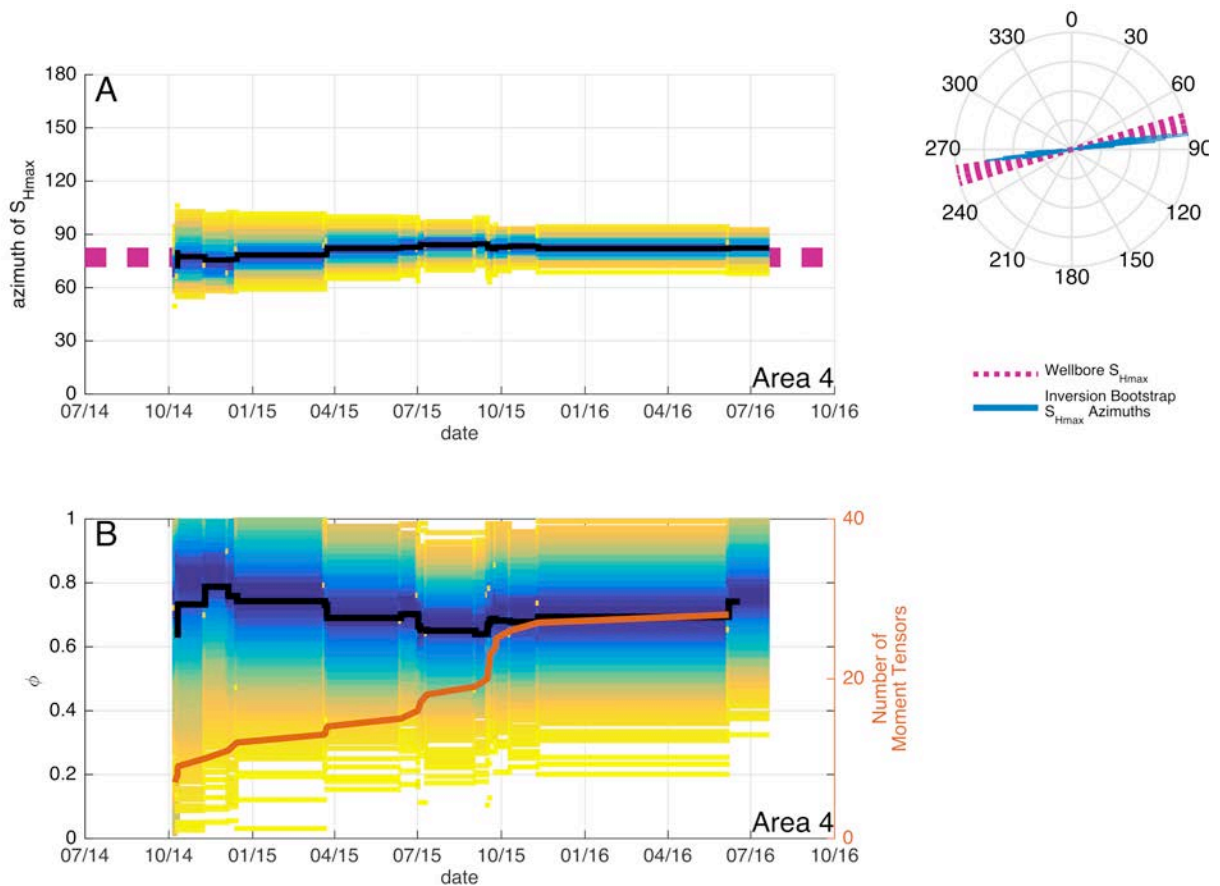


Figure DR6. Bootstrapped Inversion results through time as more earthquakes occur in area 4. Black is the deterministic inversion result, and blue-yellow shows the distribution of bootstrapped results through time. The orange line indicates the number of earthquakes with moment tensors used in the inversion as a function of time. The horizontal magenta dashed line shows the S_{Hmax} azimuths from wellbore measurements. The inversion converges to match the wellbore measurements.

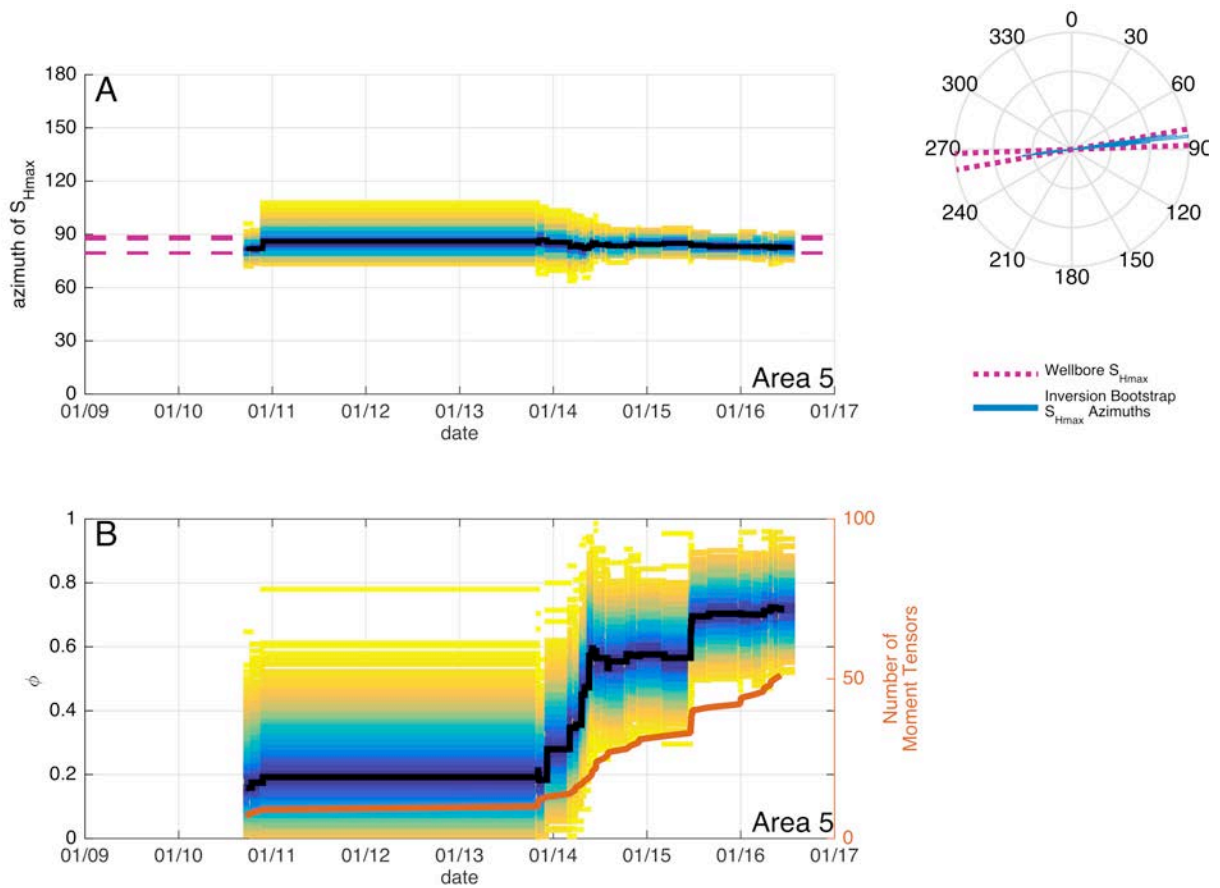


Figure DR7. Bootstrapped Inversion results through time as more earthquakes occur in area 5. Black is the deterministic inversion result, and blue-yellow shows the distribution of bootstrapped results through time. The orange line indicates the number of earthquakes with moment tensors used in the inversion as a function of time. The horizontal magenta dashed line shows the S_{Hmax} azimuths from wellbore measurements. The inversion converges to right between the two wellbore measurements.

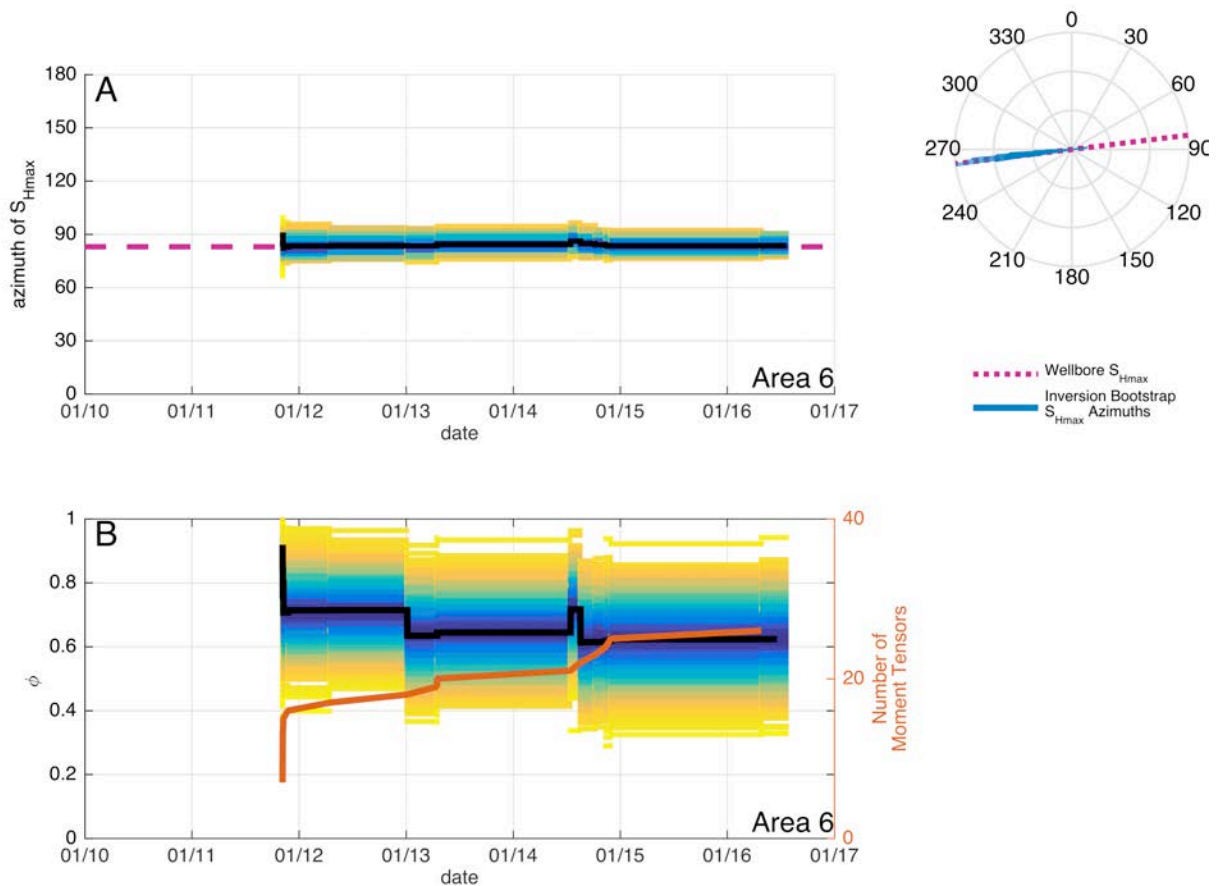


Figure DR8. Bootstrapped Inversion results through time as more earthquakes occur in area 6. Black is the deterministic inversion result, and blue-yellow shows the distribution of bootstrapped results through time. The orange line indicates the number of earthquakes with moment tensors used in the inversion as a function of time. The horizontal magenta dashed line shows the S_{Hmax} azimuths from wellbore measurements. The inversion converges to match the wellbore measurement.

Constraining Geomechanical Parameters and Their Uncertainties

The QRA propagates uncertainties in the geomechanical parameters, and it is thus only as good as the constraints in those parameters are. Here we describe how we constrain each distribution, as shown in Figure 2 for area 6, and Figures DR 9-DR13 for the other areas. The

friction distribution (Plot A) is taken from laboratory friction measurements on wet Westerly granite (Blanpied et al. 1995) at pressure and temperature. It would be ideal to have laboratory testing of the actual rock in question, but this is not available. The overburden gradient distribution (Plot G) is estimated from typical densities of sediments. The S_{Hmax} and S_{Hmin} magnitude distributions (Plots F and H) are calculated from the overburden gradient, pore pressure, ϕ , and coefficient of friction, assuming that pore pressure perturbations of less than 2 MPa are inducing slip on the faults that are most favorably oriented for failure in the current stress field. 2 MPa is a likely upper bound for pressure changes in the Arbuckle formation from wastewater injection because wellhead pressures rapidly return to subhydrostatic values after pumping stops (Nelson et al. 2015). The natural pore pressure distribution (Plot E) is uniform based on bounds from Nelson et al. (2015). Calculations are done for a depth of 5 km, the depth of most of the earthquakes in the area (McNamara et al., 2015). The distribution of fault strike (Plot D) represents the fault segments mapped within the study area with Gaussian noise of standard deviation of 2 degrees (and truncated at 5 degrees) added to each mapped strike. This can simulate non-planarity of the fault or uncertainty in mapping. Fault strikes also randomly flip 180 degrees to maintain a right hand rule between strike and dip direction, as absent constraining information, the fault can dip either direction relative to the mapped fault segment. The fault dip distribution (Plot C) is designed to sample reasonable dips of possibly active faults in a given stress state. Table DR2 shows uncertainties associated with each parameter for area 6. The main difference between these distributions in the other areas is that the unconstrained dip distribution was designed to sample the dips of active faults in in the stress state of each area.

Table DR2. Data distributions for Area 6.

Parameter	Distribution	Mean Value	Standard Deviation	Bounds	Notes
Coefficient of friction	Truncated Gaussian	0.71	0.026	0.62 to 0.82	Distribution of 23 Measurements from Blanpied et al. (1995)
Phi	Inversion bootstrap result	0.622	0.089	0.26 to 0.96	From Moment Tensor Inversion
Fault dip	Truncated Gaussian	89	10	0 to 90 degrees	Designed to sample strike-slip fault dips
Fault strike	From Map	Mapped Value	2 degrees	+/- 5 degrees	Noise added to simulate non-planarity or map uncertainty
Pore pressure	Uniform	N/A	N/A	45.2 to 50.9 MPa	Bounds from Nelson et al. (2015)
S_{hmin}	Calculated	76.6	3.18	67.0 to 91.7 MPa	Calculated from other parameters assuming frictional equilibrium
Overburden Gradient	Calculated	125	2.78	114.4 to 135.8 MPa	Based on assumed rock density
S_{Hmax}	Calculated	155.42	10.76	125.3 to 217.7 MPa	Calculated from other parameters assuming frictional equilibrium
Stress orientation	Inversion bootstrap result	N/A	N/A	N/A	From Moment Tensor Inversion

The following figures show Monte Carlo input distributions (as in Figure 3), for study areas other than Area 6.

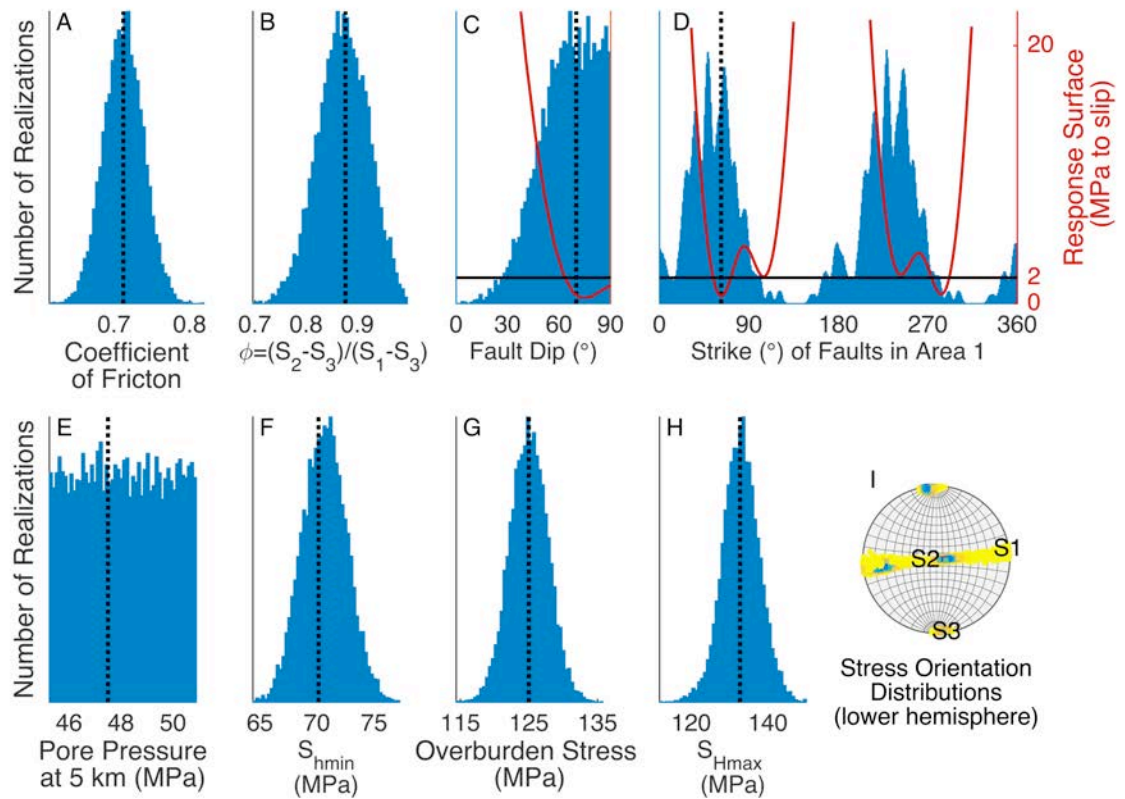


Figure DR9. Data distributions and strike and dip response surfaces for area 1. Because this is a strike slip/normal faulting transitional stress state, S_1 and S_2 can each be the steeper dipping principal stress, as evidenced by the girdle on the stereonet (I).

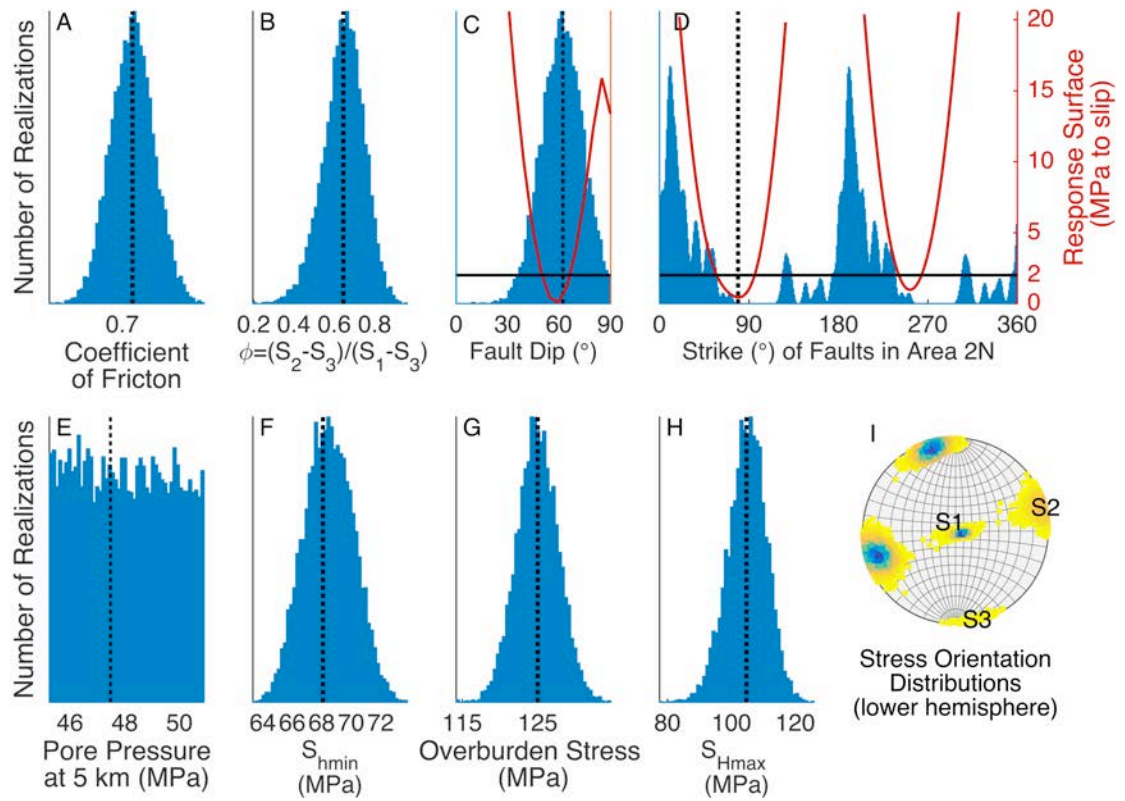


Figure DR10. Data distributions and strike and dip response surfaces for area 2N.

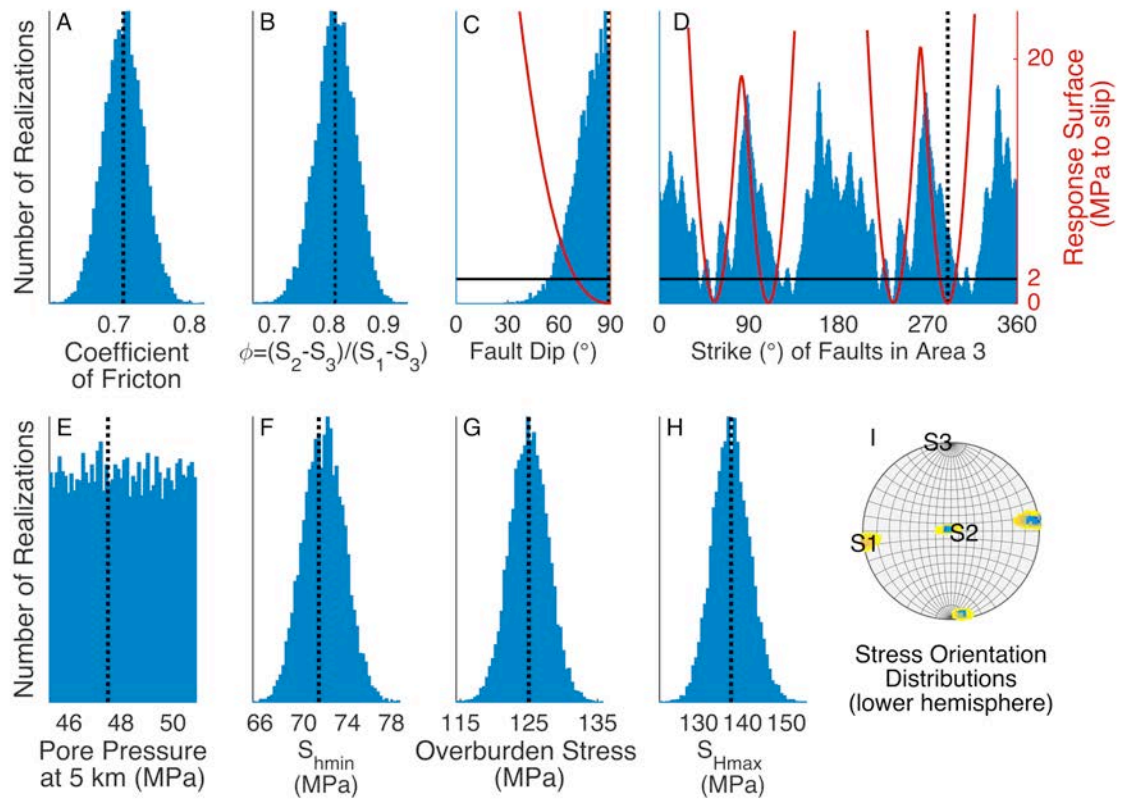


Figure DR11. Data distributions and strike and dip response surfaces (red) for area 3.

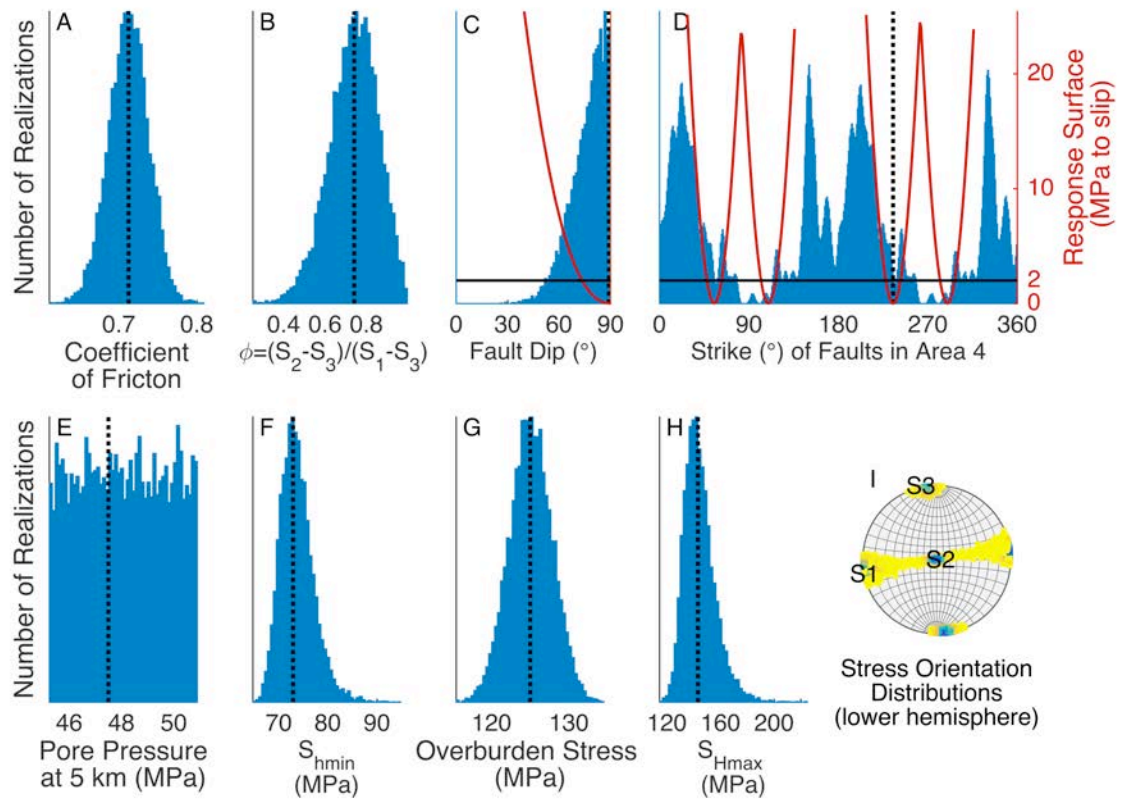


Figure DR12. Data distributions and strike and dip response surfaces (red) for area 4.

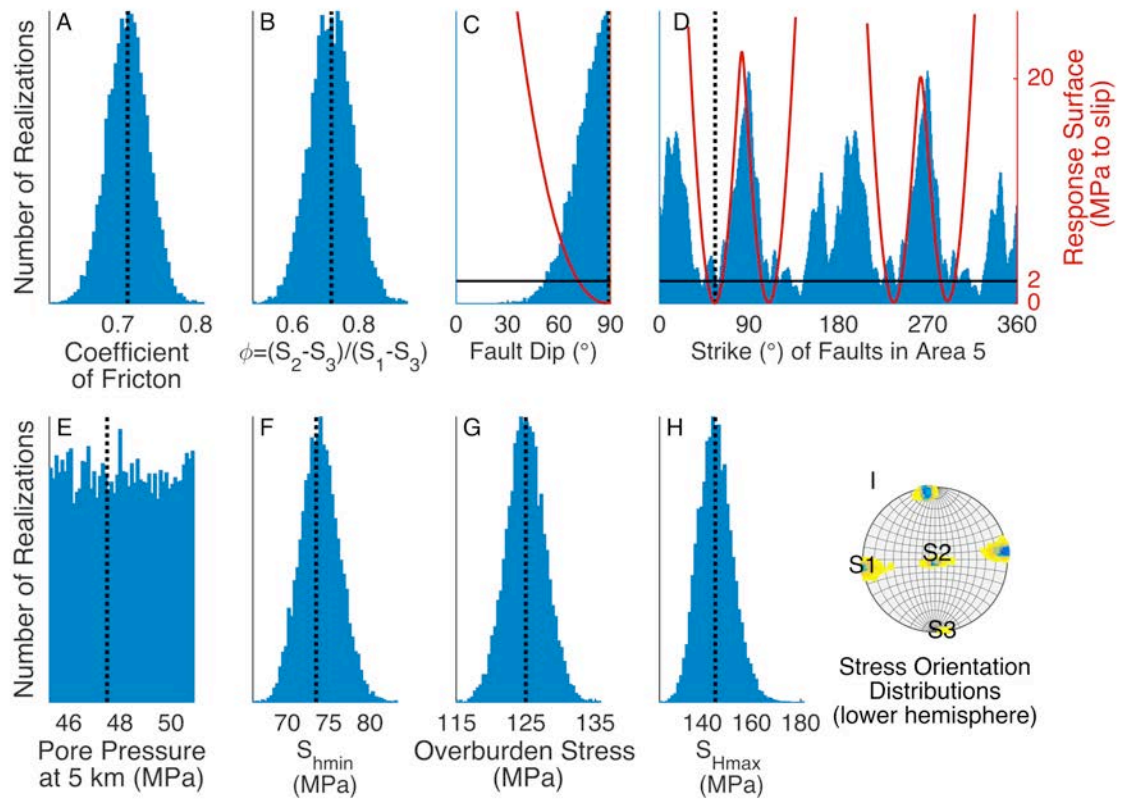


Figure DR13. Data distributions and strike and dip response surfaces for area 5.

Below are traffic light colored mapped faults in each study area (A), and their corresponding CDF curves in B. Panel C extends the pressure axis to pressure ranges that would be more applicable to hydraulic fracturing induced seismicity and shows the fracture gradient.

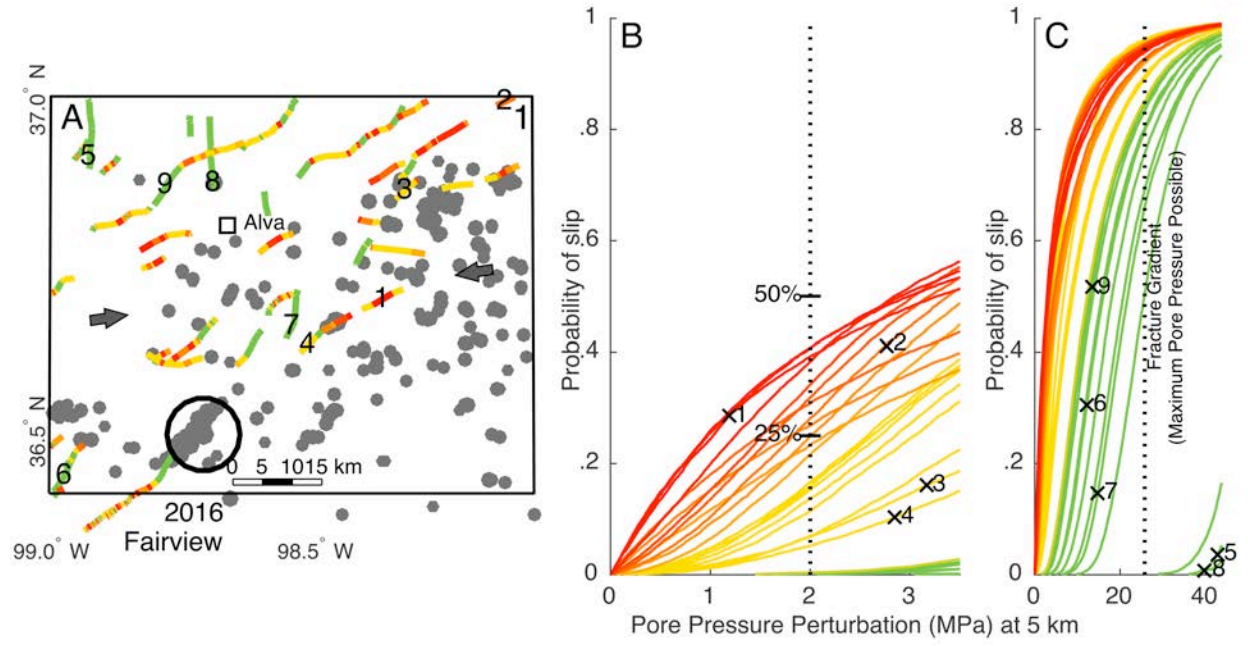


Figure DR14. Faults, NEIC earthquakes (A), and CDF curves (B, C) for area 1.

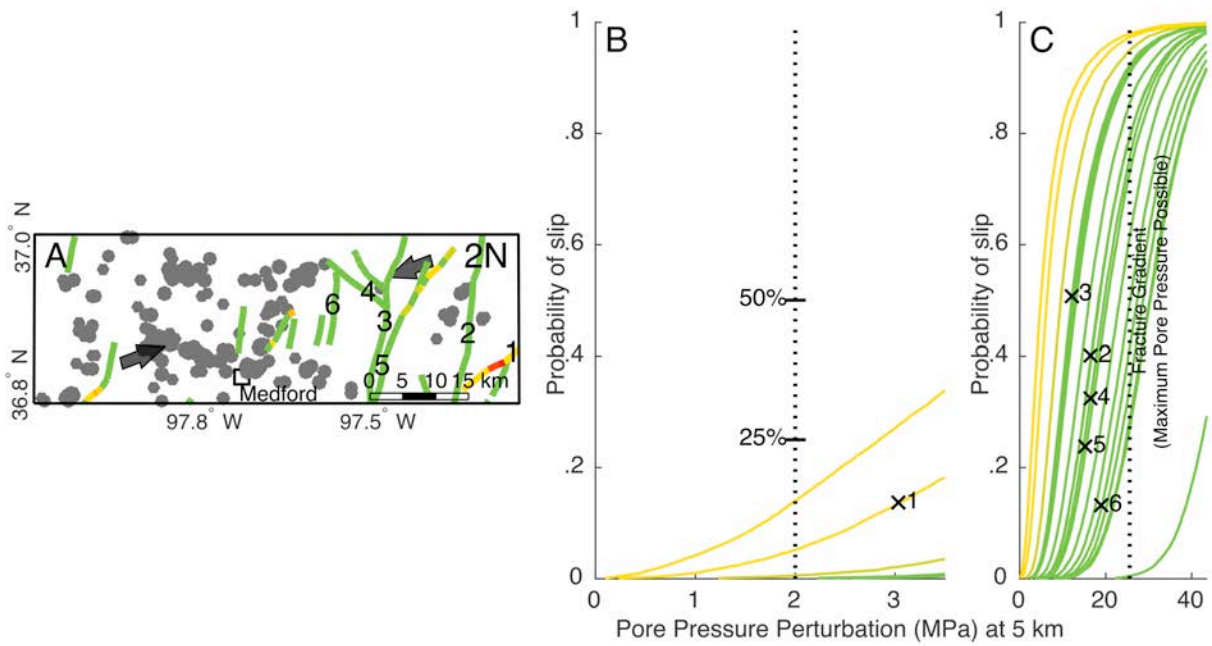


Figure DR15. Faults, NEIC earthquakes (A), and CDF curves (B, C) for area 2N.

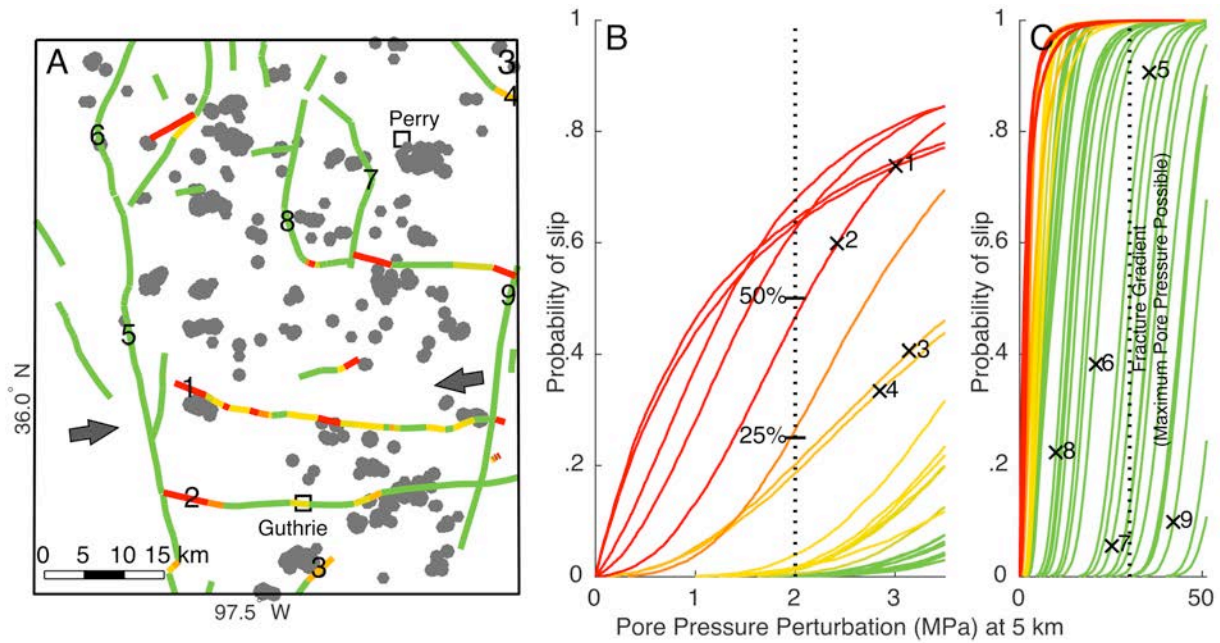


Figure DR16. Faults, NEIC earthquakes (A), and CDF curves (B, C) for area 3.

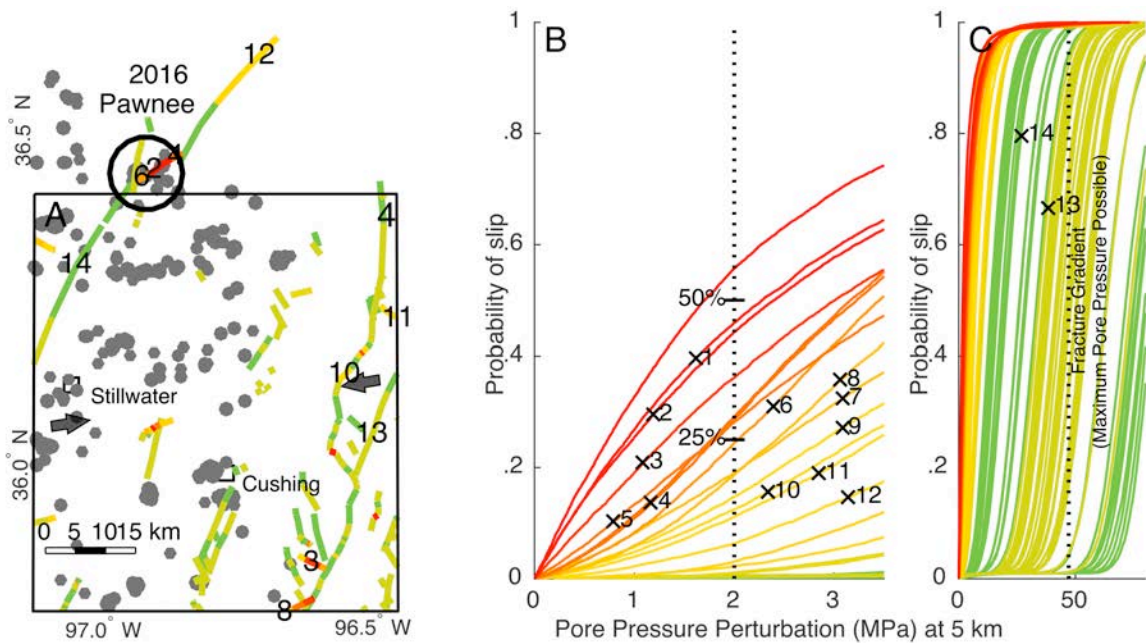


Figure DR17. Faults, NEIC earthquakes (A), and CDF curves (B, C) for area 4. The September 2016 Pawnee Magnitude 5.8 happened near a mapped fault just outside of area 4. When extend the area 4 analysis, we see fault segments 6, 2, and 4, from south to north, colored varying shades of orange and red. Their CDF curves are numbered correspondingly in panel B. Note that

this analysis is done with earthquakes up to 2 months before the magnitude 5.8, so it was not used in the inversion. The main event occurred on an unmapped fault conjugate to the mapped fault. Had it been mapped, it would have been colored red too.

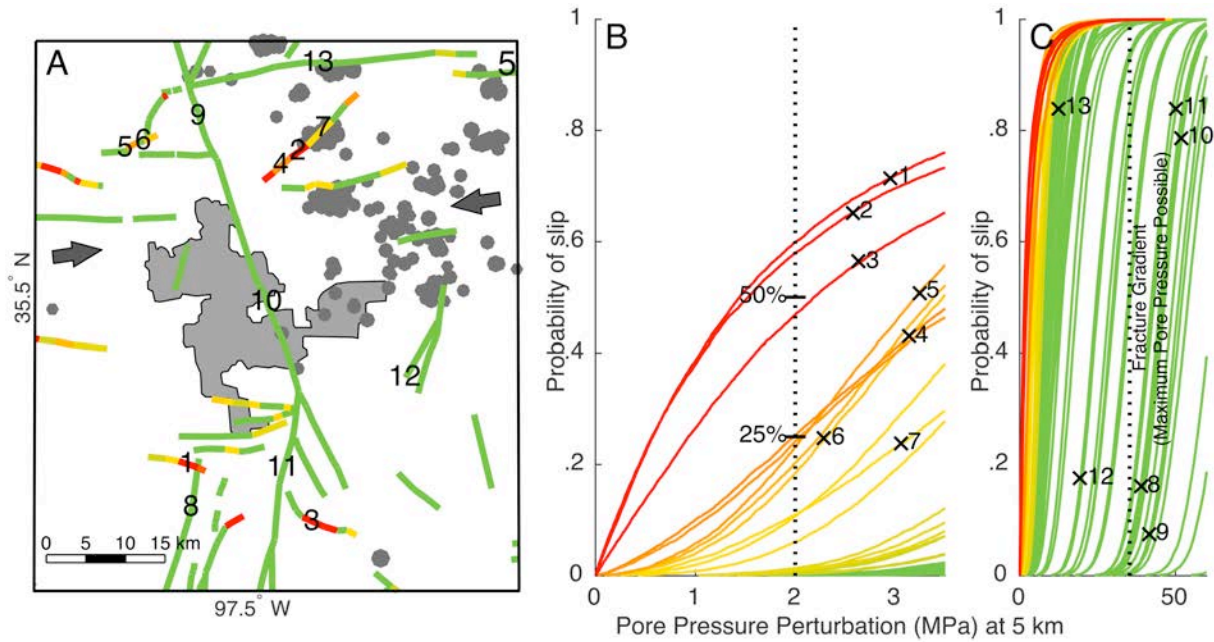


Figure DR18. Faults, NEIC earthquakes (A), and CDF curves (B, C) for area 5. The Oklahoma City urban area is outlined in grey.

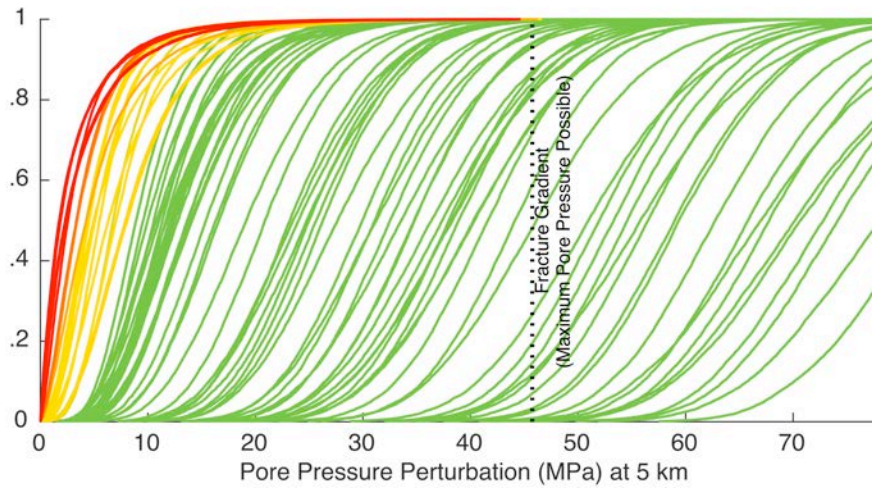


Figure DR19. CDF curves for study area 6 on an extended pressure axis.

REFERENCES CITED

- Blanpied, M. L., Lockner, D. A., Byerlee, J. D., 1995, Frictional slip of granite at hydrothermal conditions: *Journal of Geophysical Research* v. 100, no. B7, p. 13,045-13,064.
- Friberg, P. A., Besana-Ostman, G. M., and Dricker, I., 2014, Characterization of an earthquake sequence triggered by hydraulic fracturing in Harrison County, Ohio: *Seismological Research Letters* v. 85, no. 6 doi: 10.1785/0220140127
- Ellsworth, W. L. 2013, Injection-induced earthquakes: *Science*, 12 Jul, 2013: V. 341: I. 6142. DOI: 10.1126/science.1225942
- Holland, A. A., 2013 Earthquakes triggered by hydraulic fracturing in south-central Oklahoma: *Bulletin of the Seismological Society of America* v. 103, no. 3 p. 1784-1792.
- Nelson, P. H., Gianoutsos, N. J., and Drake II, R. M., 2015, Underpressure in Mesozoic and Paleozoic rock units in the Midcontinent of the United States: *AAPG Bulletin*, v. 99, no. 10 pp. 1861–1892, DOI: 10.1306/04171514169.
- NRC (National Research Council), *Induced Seismicity Potential in Energy Technologies* (The National Academies Press, Washington, DC, 2012).
- Twiss, R.J., and Moores, E. M., 1992, *Structural Geology*, W. H. Freeman and company, 532 p.